using the BOLPs-RGp. The position and intensity of activity were measured during the 200 s immediately after proton irradiation using the trigger signal of the beam-off time. The measurement was performed using the shortest possible distance between the two opposing detector heads of the BOLPs-RGp for each patient. The average distance of the detector heads was 40 cm for the head and neck and the brain, 70 cm for the liver and the lungs, and 50 cm for the prostate. The time of 200 s after proton beam irradiation was chosen according to the intensity of activity estimated from the results of other studies (10, 13). The activity data obtained during proton irradiation were not used for PET imaging. Various types of background radiation (X-rays, gamma rays, and neutrons) occur during proton beam irradiation, and the quality of the activity image becomes markedly worse in their presence (2, 10, 15, 16). Furthermore, high radiation decreases the accuracy of the detector.

Verification of activity measurement was performed in 18, 4, 15, 10, and 1 cases involving tumors of the head and neck, the liver, the lungs, the prostate, and the brain, respectively. The typical fractional dose is 2.5 Gy equivalents (GyE = Gy × the relative biologic effectiveness: [= 1.1 = constant]) for the head and neck, 3.8 GyE for the liver, 4.0 GyE for the lungs, 2.0 GyE for the prostate, and 2.5 GyE for the brain in our facility. The irradiated field is typically planned with three fields in the head and neck and two fields in other sites. Furthermore, the typical number of irradiated field per fractional dose is one in the head and neck, liver, and prostate, and two in the lungs. The fractional dose was delivered over an irradiation time of 10–300 s. The proton beam irradiation was synchronized with the organ motion caused by respiration in the liver and the lungs.

*Procedure for clinical use of activity image*

A flow chart of procedure for clinical use of the BOLPs-RGp is shown in Fig. 2. In the clinical use, the main operation is to take an activity image every day and compare the activity image of the first day of treatment with each activity image during the comparatively long period of the treatment. If the difference of both the images is confirmed by reducing of the tumor size and changing of the body shape, then the new dose distribution is obtained from redose calculation of the plan on a new CT image acquisition, and the first proton treatment plan is immediately corrected to the new plan. As a result, proton treatments of high accuracy can be offered to the patient by keeping of the planned dose delivery.

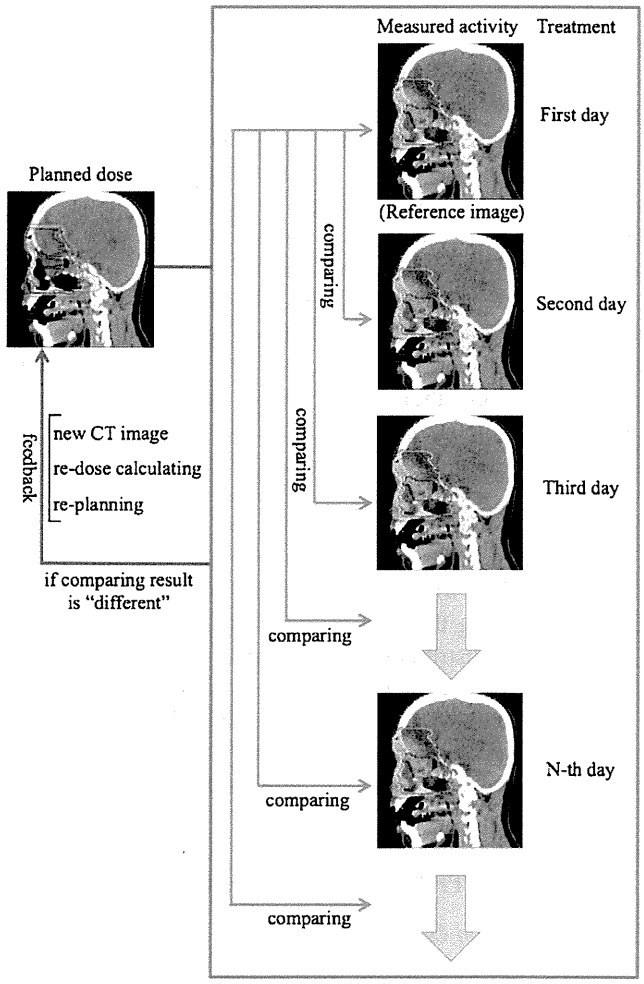


Fig. 2. Flow diagram of the procedure for the clinical use of the BOLPs-RGp.

## RESULTS

*Estimation of the measurement time for PET imaging*

An estimation of an appropriate measurement time for PET imaging was performed using the measured activity data from tumors of the head and neck. The proton beam conditions were as follows: an energy of 120 MeV, a spread out of Bragg peak (SOBP) of 80-mm width, a gantry angle of 340°, a fractional dose of 2.5 GyE, and an irradiation time of 24 s. The distance between the detector heads was 70 cm, and the detection rate of the activity was 1.5 kcps. The left panel of Fig. 3 shows the number of detection events per volume during the detection period after proton beam irradiation. The statistical error (= standard deviation/mean value) decreased as the detection time increased. The error was 2.8% for a 200-s detection time, 3.0% for 150 s, 3.4% for 100 s, and 4.4% for 50 s. The right panel of Fig. 3 shows PET images taken using detection times of (a) 0, (b) 50, (c) 100, and (d) 200 s.

*PET images of each treatment site*

Typical PET images obtained by the BOLPs-RGp are shown for each case involving tumors of the head and neck, the liver, the lungs, the prostate, and the brain. Figure 4 shows the calculated dose distribution and the measured activity distribution on the first treatment day. The beam irradiation parameters were shown in Table 1. The PET images were obtained during the 200 s after proton beam irradiation. The mean detection rates of the activity generated in the proton beam irradiated volume were 1.58, 1.39, 0.53, 1.08, and 1.85 kcps, respectively. The color line and wash normalized to the iso-center show the dose distribution and activity distribution, respectively. By comparing and verifying between the calculated dose distribution and the measured activity distribution, it can be confirmed visually and roughly that the proton beam has irradiated the tumor. In cases of the liver and the lungs, the length of beam irradiation time is adjusted according to the stability of respiration on the treatment day and the patient. By the effect of organ motion, the number of

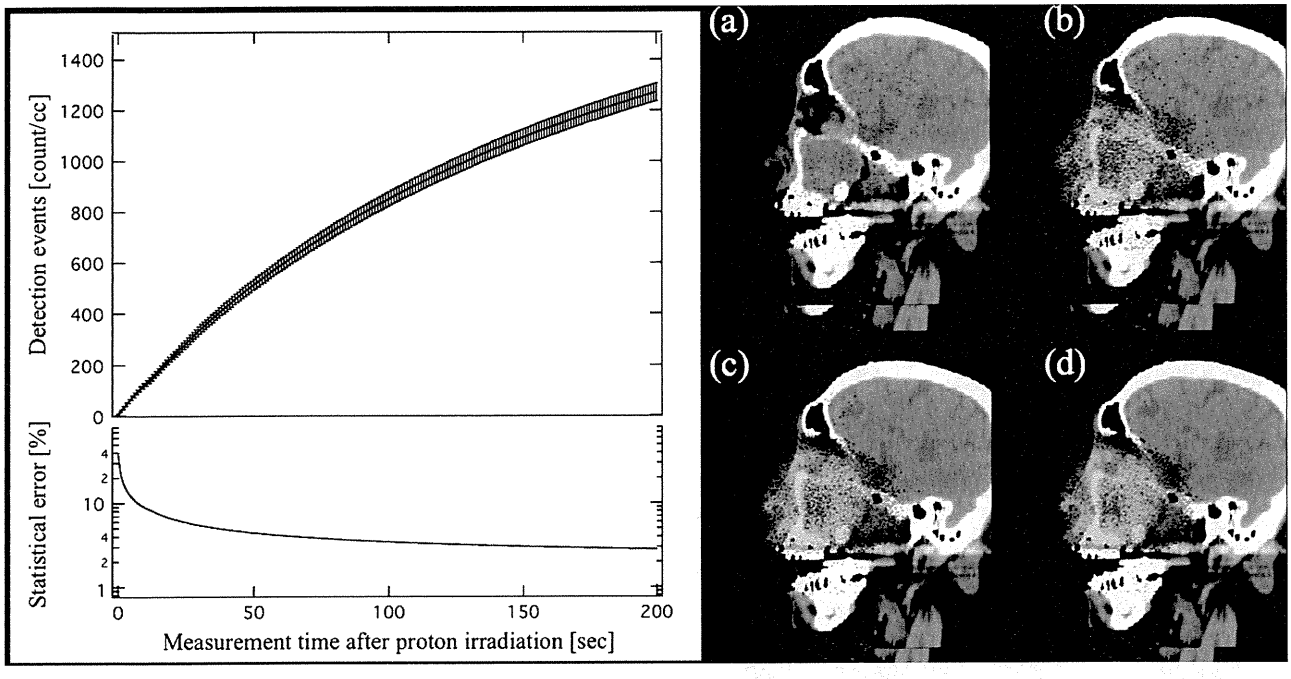


Fig. 3. The number of detection events per volume and PET images obtained during the detection period after proton beam irradiation. The PET images for detection period of (a) 0, (b) 50, (c) 100, and (d) 200 s are shown.

the detection event of the activity measured in the gating window will became about one third of the total detection events, and the statistical error will increase. Therefore, the measurement was performed with no synchronization with organ motion by respiration.

*Changes in the activity distribution during the treatment period*

In each treatment site, the activity distribution changed probably by reduction of the tumor size and changing of the body shape was conspicuously observed in some cases of the head and neck.

The verification was performed for a case involving tumors of the head and neck. Proton beam irradiation was performed in three fields of view: Port 1: 123 MeV, 90-mm SOBP, 350° gantry angle, 0° bed angle; Port 2: 121 MeV, 90-mm SOBP, 10° gantry angle, 20° bed angle; and Port 3: 117 MeV, 80-mm SOBP, 340° gantry angle, 350° bed angle. The irradiation dose was 2.5 GyE. Figure 5 shows a calculated proton dose distribution, an activity distribution, and a depth profile of a 2.5-GyE dose irradiation after a delivery dose of 2.5 (reference image), 10.0, 17.5, or 32.5 GyE from Port 1, a delivery dose of 5.0 (reference image), 12.5, 20.0, or 35.0 GyE, from Port 2, and a delivery dose of 7.5 (reference image), 15.0, 22.5, or 30.0 GyE from Port 3. Changes of the activity distribution were observed according to changes of the proton beam range and the dose delivered by previous irradiations resulted in a reduction of the tumor (see the arrow and the area surrounded by the dotted line in Fig. 5). The changing values of the activity range for each irradiation field (Port 1, Port 2, and Port 3) are shown in upper left of Fig. 6. The activity range was defined by the depth point of 50% distal falloff in the activity distribution normalized at the iso-center. The changing value of the activity range fully exceeded a 10-mm length. Moreover, to observe the changes in the activity distribution in the depth direction in a similar manner, the ratio of the integration of the detected numbers between 20 mm and 70 mm from the iso-center was expressed as follows:

$$R(D) = \frac{\int_{20}^{70} \left(dA(D)/dZ\right) dz}{\int_{20}^{70} \left(dA(0)/dZ\right) dz}. \quad (1)$$

Here, $z$ is the depth, D is the delivery dose, A(D) is the depth activity distribution, and A(0) is the reference depth activity distribution. The ratio of the delivery dose is shown in the middle left of Fig. 6. The bottom left of Fig. 6 is the proton beam irradiation time per fraction dose at each irradiation. The average of the irradiation time was 30 s, and the difference of the irradiation time at random was within 3 s.

In this case, a new CT image was scanned and a retreatment planning was produced after the delivery of 35 GyE of the prescribed dose of 65 GyE. The volume of the tumor was decreased from 184 mL to 125 mL (the arrow in right of Fig. 6 shows the visible tumor reduction), and the maximum beam range was shortened by 20-mm water equivalent length. In the other 2 cases of 18 clinical cases of the head and neck, the changing activity range of more than 10 mm was observed. Similarly, the new CT image acquisition and the retreatment planning were immediately performed after the observation of the changing activity range. The reduction

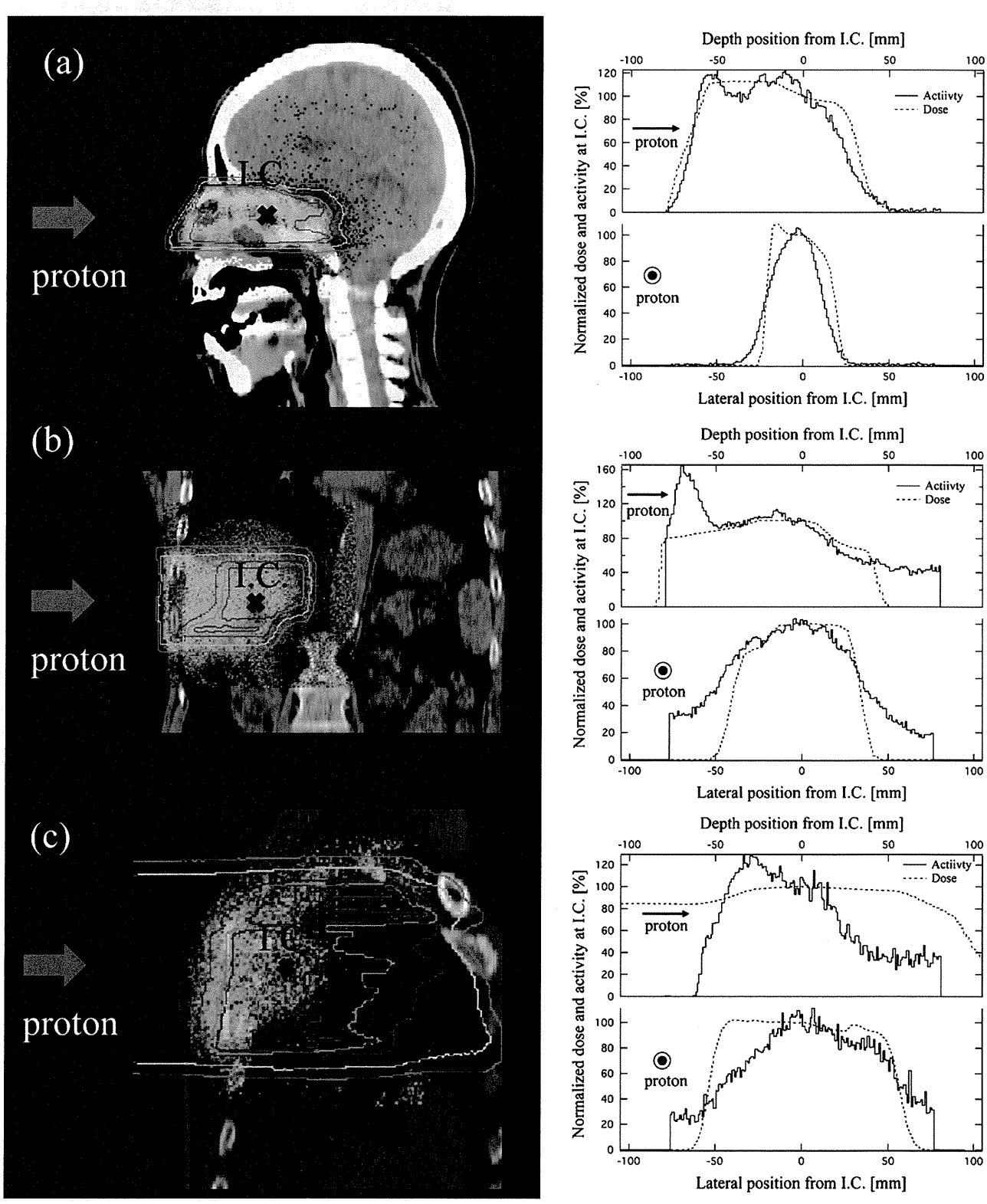


Fig. 4. The calculated dose distribution and the measured activity distribution (left figure), and corresponding lateral and depth profiles (right figure) of the irradiation fields (see Table 1) in each case involving tumors of the head and neck (a), the liver (b), the lungs (c), the prostate (d), and the brain (e), respectively. The iso-dose line of 100% is red, 80% yellowish green, 50% light blue, and 20% purple. The iso-activity wash between 30% and 100% changed from light blue to red.

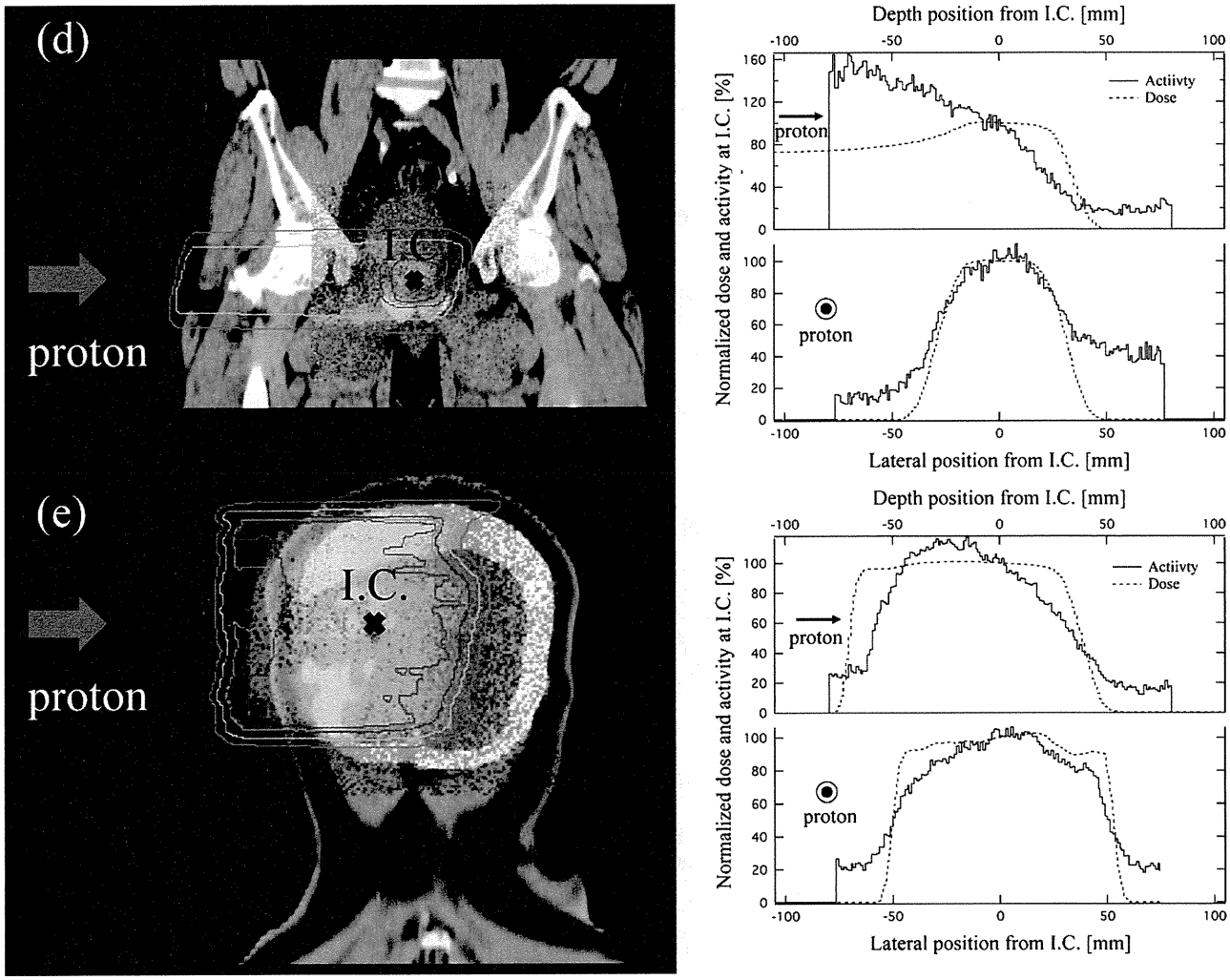


Fig. 4. (*continued*).

of the tumor's volume was more than 100 mL. Also, in carbon therapy, similar observation of the tumor shrinkage has been reported in (7). The BOLPs-RGp indicated that the proton irradiation dose was delivered to the brain stem of organs at risk.

*Washout effect of the activity in the treatment period*

A histopathologic examination demonstrated that higher activity was observed in regions containing necrotic liver cells than in any other region. The upper panel of Fig. 7 shows the calculated dose distribution and the measured activity distribution on a CT image taken at the first treatment of a 3.8 GyE delivery dose. The bottom left panel of Fig. 7 shows the number of detection counts per 20 s of activity in the regions of interest of areas A and B in the liver. Hence, the region of interest of area A is the necrotic region of the tumor, and area B is the normal tumor region. Therefore, area B-A is equivalent to the area of the tumor minus the necrotic region. The observed decay curves in the region of interest of area A and B-A were fitted well enough using a double exponential equation. The two half-lives of the double exponential fitting were 31 $\pm$ 8 s and 146 $\pm$ 20 s in the area A, and 21 $\pm$ 4 s and 164 $\pm$ 11 s in the area B-A, respectively. The half-life was longest in the necrotic region of the tumor. The activity images for the 200 s measurement by the BOLPs-RGp are shown in the left of Fig. 8. The high activity

Table 1. Summary of proton beam irradiation parameters

| | Treatment site | Proton energy [MeV] | SOBP [mm] | Gantry angle [deg.] | Bed angle [deg.] | Fractional dose [GyE] | Irradiation time [sec.] |
|---|---|---|---|---|---|---|---|
| (a) | Head and Neck | 123 | 90 | 0 | 0 | 2.5 | 39 |
| (b) | Liver | 137 | 70 | 270 | 0 | 3.8 | 229 |
| (c) | Lungs | 145 | 70 | 160 | 0 | 2.0 | 38 |
| (d) | Prostate | 187 | 50 | 270 | 0 | 2.0 | 15 |
| (e) | Brain | 122 | 90 | 330 | 90 | 2.5 | 40 |

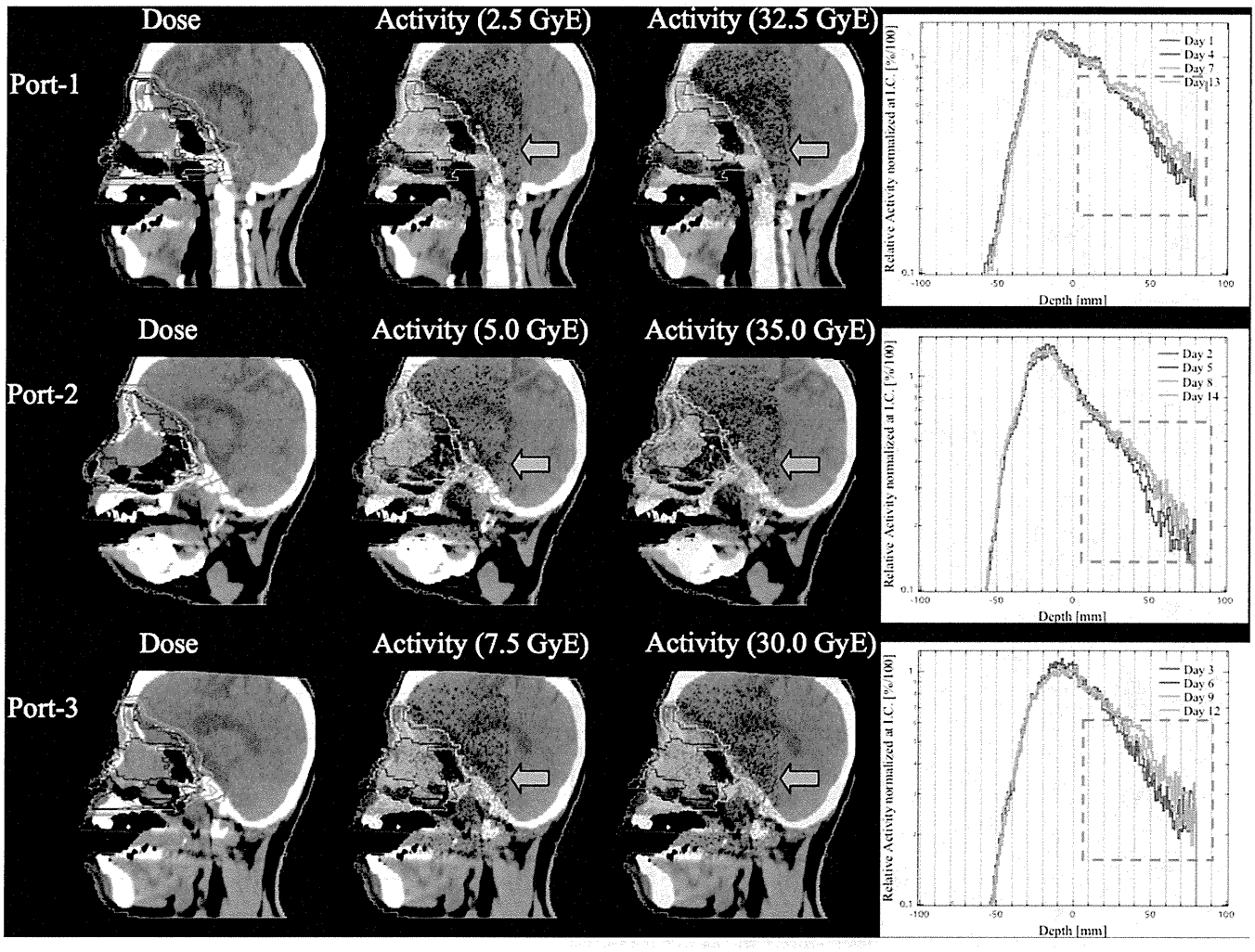


Fig. 5. The calculated proton dose distribution, measured activity distribution of a 2.5-GyE dose irradiation, and the depth profile of the measured activity normalized to the iso-center (0-mm depth) of the reference activity after a delivery dose of 2.5–35.0 GyE.

of the necrotic region decreased to same level as the normal parts of the liver in the last treatment. The ratio F of the detection activity normalized to the activity data from the first treatment for the delivery doses in the area A and the area B-A is expressed as follows:

$$F(D) = \frac{\int_0^{S_A} (dN(D)/dS)\, dS / \int_0^{S_A} dS}{\int_{S_A}^{S_B} (dN(D)/dS)\, dS / \int_{S_A}^{S_B} dS}. \quad (2)$$

Here, N is the detection number, $S_A$ is the square of area A, and $S_B$ is the square of area B. Ratio of the F values normalized at the value in first treatment calculated by using Eq. 2 and proton beam irradiation time per fraction dose are shown in the right of Fig. 8. The average of the irradiation time at random was 159 ± 77 s. There was no correction in the irradiation time and the decrease of the activity shown in Fig. 8. A decrease in the activity of the necrotic region was observed after the delivery dose was increased without depending on the beam irradiation time per fraction dose.

## DISCUSSION

This study focused on the development of the BOLPs-RGp and its clinical use against tumors of the head and neck, liver, lungs, prostate, and brain in the proton therapy. Quick measurement of the activity generated in a patient's body after proton irradiation is feasible by using the BOLPs-RGp. The elements tracked by the activity imaging are $^{11}C$ (20.39 min), $^{10}C$ (19.26 s), $^{13}N$ (9.965 min), $^{15}O$ (122.2 s), $^{14}O$ (70.61 s), $^{30}P$ (2.498 min), and $^{38}K$ (7.636 min), and according to the results of a simulation by Parodi *et al.*, the "key" positron emitter nuclei are $^{11}C$ and $^{15}O$ (14). The measurement of this activity must be immediately performed after proton irradiation as the half-life of $^{15}O$ is about 2 min. As a result, the information for activity imaging is obtained in a short period. On the other hand, in the case of a beam OFF-LINE PET system used with a commercial based PET or PET/CT apparatus, it is very difficult to measure the activity of $^{15}O$ for several minutes even at the start of the activity measurement after proton irradiation. The main elements used for activity imaging are $^{15}O$ for measurements with

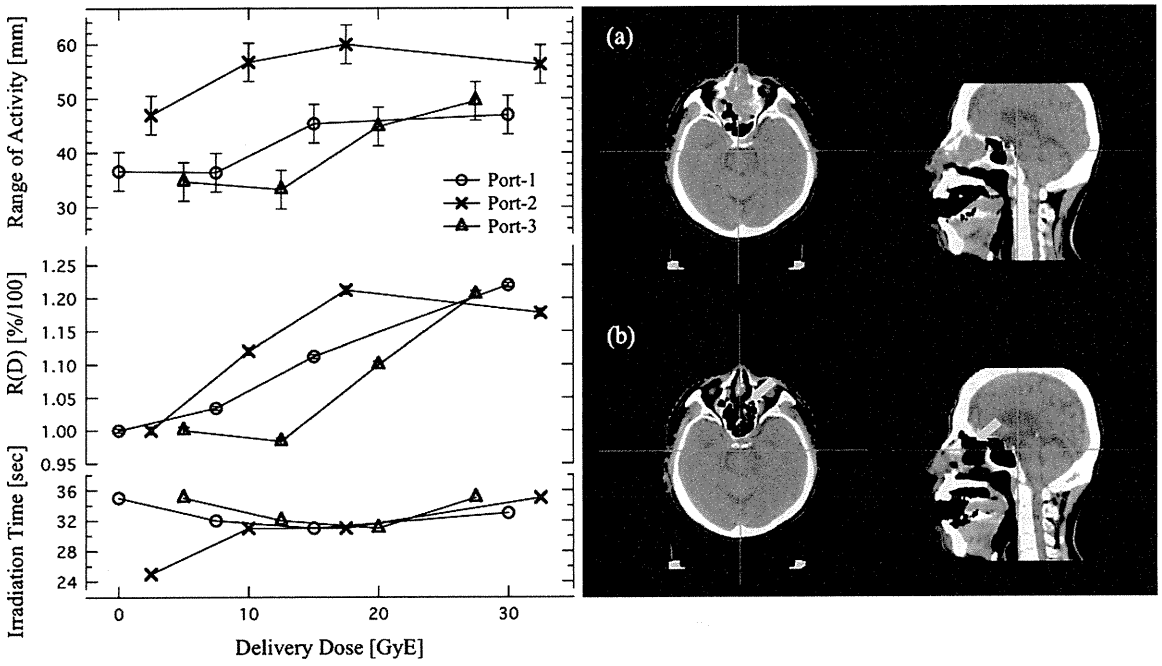


Fig. 6. Changes in the values of the activity range and proton beam irradiation time per fraction dose at each irradiation field of Port-1, Port-2, and Port-3. Axial and sagittal CT images of the head and neck before treatment (a) and after delivery doses of 35 GyE (b).

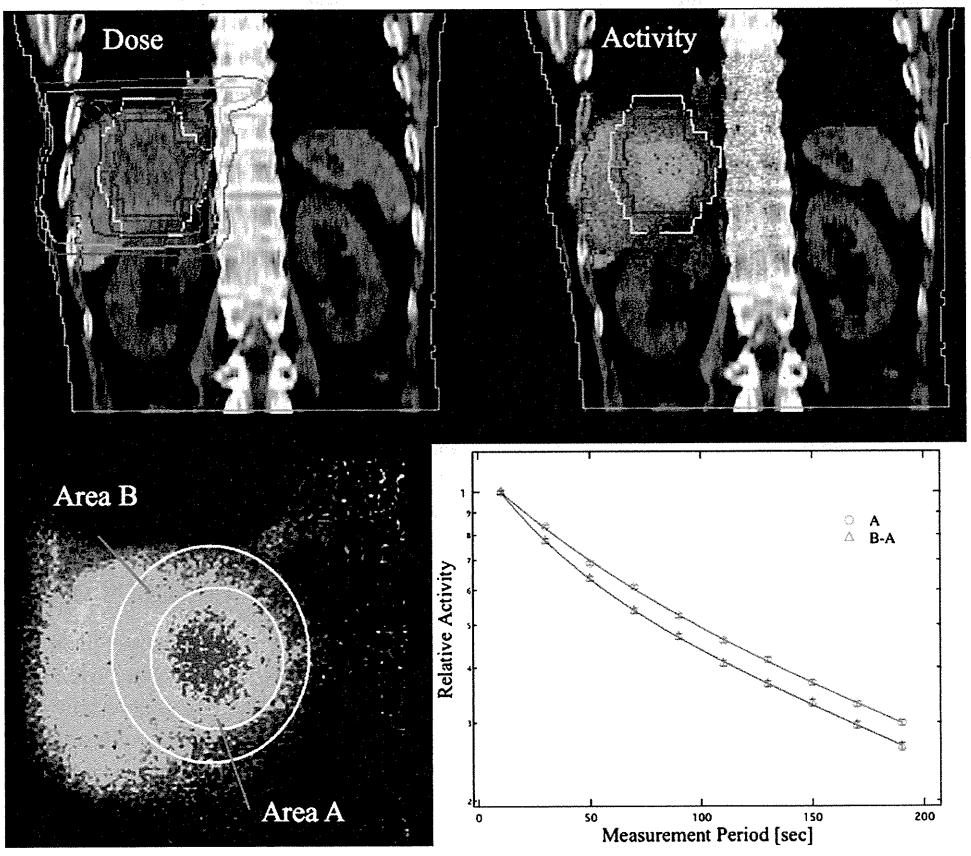


Fig. 7. The calculated dose distribution and the measured activity distribution on a CT image after the first treatment with a 3.8-GyE delivery dose, and the number of detection counts per 20 seconds of the activity in the region of interest (ROI) of areas A and B in the liver.

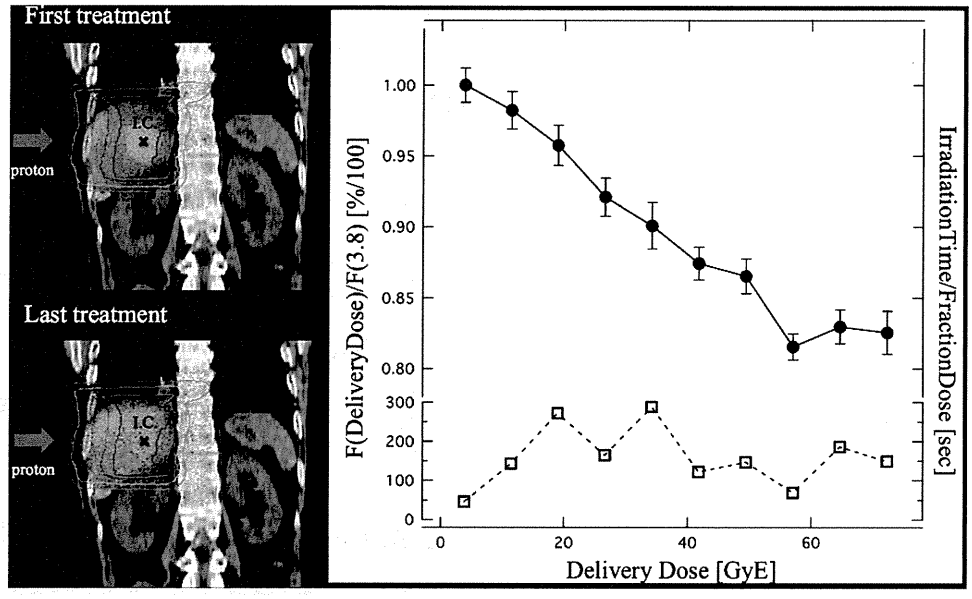


Fig. 8. The activity image and the ratio of the detection number to the measured activity calculated according to Equation (2) in the necrotic region of the liver tumor, and proton beam irradiation time per fractional dose.

the BOLPs-RGp and $^{11}C$ for measurements with the beam OFF-LINE PET system. As a tumor is equivalent to soft tissue, the measurement of the many $^{15}O$ nuclei generated in a tumor by proton irradiation is very important for the observation and evaluation of the changing form and the delivery dose response of the tumor. $^{12}C$ is present and $^{11}C$ is generated in the adipose tissue. Therefore, high activity is indicated in the region under the skin when using the beam OFF-LINE PET system. Furthermore, the BOLPs-RGp has the advantage of taking measurements with the patient in same position during proton irradiation. However, the CT image for the patient positioning can not be acquired at the same time as the activity measurement when using the BOLPs-RGp. This problem can be solved by the technological introduction of a CBCT.

At present, the length of activity measurement with the BOLPs-RGp after proton beam irradiation is 200 s; but, it may be possible that the measurement time can be shortened to less than 200 s as a result of this research. However, the measurement time must be determined with consideration to the detection efficiency by the delivery dose of each treatment site, the distance between the detector heads, and the activity measurement synchronized with the organ motion caused by respiration in the case of the liver and lungs.

The BOLPs-RGp has been used in the daily proton treatment of 48 patients. The monitoring of the accuracy of the proton beam irradiation was performed by comparing and verifying the daily activity images with reference activity images obtained at the start of the proton treatment. Specially, optimized proton treatment was performed by quickly replanning treatment in three clinical cases involving head-and-neck tumors, because different activity distribution were observed in the two images during the treatment period. The decrease of the activity in the region of necrotic cells in the liver tumor found during the histopathological examination was linked to an increase in the delivery dose. It is suggested that the increase in the washout effect in the necrotic region is caused by a decrease in the number of necrotic cells in the liver because of increased blood flow caused by the higher proton delivery dose. This effect may indicate a need to adapt the treatment to the dose response of the tumors in individual patients as well as the observation of the functional metabolism of organs.

The quality of the activity image is reduced by the large organ motion of the liver and the lungs. In cases of the prostate, the verification of changes in the activity distribution against the condition of the bladder and the position of the head of the femur will be reported in future. Moreover, a study concerning the experimental determination of cross sections of the target nuclear fragment reaction has been completed, and a simulation system that includes our cross-section data for calculating activity distribution in a patient's body with a high accuracy has been constructed using a cluster computer system. Many results of the research of the simulation have been already reported by the study group of Parodi *et al.* (12, 14). Finally, the ideal DGPT will be achieved through these developments and the research.

## CONCLUSIONS

A BOLPs-RGp was constructed in our proton treatment room. The BOLPs-RGp has been used in many clinical cases. Report of the clinical use with beam ON-LINE PET or in-beam PET in the proton therapy has been never done before. The daily activity images obtained indicated the proton irradiation volume of the treatment administered to patients. Information about the positron-emitting nuclei provided by the BOLPs-RGp will be important for improving proton treatment accuracy in the future. DGPT (10) will thereby be achieved via daily proton treatment using the BOLPs-RGp.

## REFERENCES


1. Oelfke U, Lam G, Atkins M. Proton dose monitoring with PET: Quantitative studies in Lucite. *Phys Med Biol* 1996;41: 177–196.
2. Litzenberg DW, Roberts DA, Lee MY, *et al.* On-line monitoring of radiotherapy beams: Experimental results with proton beams. *Med Phys* 1999;26:992–1006.
3. Parodi K, Enghardt W. Potential application of PET in quality assurance of proton therapy. *Phys Med Biol* 2000;45:N151–N156.
4. Nishio T, Ogino T, Shimbo M, *et al.* Distributions of $b^+$ decayed nucleus produced from the target fragment reaction in $(CH_2)n$ and patient liver targets by using a proton beam for therapy. *Abstr XXXIV PTCOG Mtg Boston* 2001;15–16.
5. Parodi K, Enghardt W, Haberer T. In-beam PET measurements of $\beta^+$ radioactivity induced by proton beams. *Phys Med Biol* 2002;47:21–36.
6. Hishikawa Y, Kagawa K, Murakami M, *et al.* Usefulness of positron-emission tomographic images after proton therapy. *Int J Radiat Oncol Biol Phys* 2002;53:1388–1391.
7. Enghardt W, Parodi K, Crespo P, *et al.* Dose quantification from in-beam positron emission tomography. *Radiother Oncol Suppl 2* 2004;73:S96–S98.
8. Nishio T, Sato T, Kitamura H, *et al.* Distributions of $\beta^+$ decayed nuclei generated in the $CH_2$ and $H_2O$ targets by the target nuclear fragment reaction using therapeutic MONO and SOBP proton beam. *Med Phys* 2005;32:1070–1082.
9. Parodi K, Ponisch F, Enghardt W. Experimental study on the feasibility of in-beam PET for accurate monitoring of proton therapy. *IEEE Trans Nucl Sci* 2005;52:778–786.
10. Nishio T, Ogino T, Nomura K, *et al.* Dose-volume delivery guided proton therapy using beam ON-LINE PET system. *Med Phys* 2006;33:4190–4197.
11. Parodi K, Paganetti H, Cascio E, *et al.* PET/CT imaging for treatment verification after proton therapy: A study with plastic phantoms and metallic implants. *Med Phys* 2007;34: 419–435.
12. Parodi K, Paganetti H, Shih HA, *et al.* Patient study of in vivo verification of beam delivery and range, using positron emission tomography and computed tomography imaging after proton therapy. *Int J Radiat Oncol Biol Phys* 2007;68:920–934.
13. Nishio T, Miyatake A, Inoue K, *et al.* Experimental verification of proton beam monitoring in a human body by use of activity image of positron-emitting nuclei generated by nuclear fragmentation reaction. *Radiol Phys Technol* 2008;1: 44–54.
14. Parodi K, Ferrari A, Sommerer F, *et al.* Clinical CT-based calculations of dose and positron emitter distributions in proton therapy using the FLUKA Monte Carlo code. *Phys Med Biol* 2007;52:3369–3387.
15. Pawelke J, Enghardt W, Haberer T, *et al.* In-beam PET imaging for the control of heavy-ion tumour therapy. *IEEE Trans Nucl Sci* 1997;44:1492–1498.
16. Parodi K, Crespo P, Eickhoff H, *et al.* Random coincidences during in-beam PET measurements at microbunched therapeutic ion beams. *Nucl Instrum Meth A* 2005;545:446–458.
17. Uchida H, Okamoto T, Ohmura T, *et al.* A compact planar positron imaging system. *Nucl Instr Meth* 2004;A516:564–574.

Radiol Phys Technol
DOI 10.1007/s12194-010-0084-z

# Evaluation of the usefulness of a MOSFET detector in an anthropomorphic phantom for 6-MV photon beam

**Ryosuke Kohno · Eriko Hirano · Satoshi Kitou · Tomonori Goka · Kana Matsubara · Satoru Kameoka · Taeko Matsuura · Takaki Ariji · Teiji Nishio · Mitsuhiko Kawashima · Takashi Ogino**

Received: 23 July 2009 / Revised: 7 January 2010 / Accepted: 8 January 2010


**Abstract** In order to evaluate the usefulness of a metal oxide-silicon field-effect transistor (MOSFET) detector as a in vivo dosimeter, we performed in vivo dosimetry using the MOSFET detector with an anthropomorphic phantom. We used the RANDO phantom as an anthropomorphic phantom, and dose measurements were carried out in the abdominal, thoracic, and head and neck regions for simple square field sizes of 10 × 10, 5 × 5, and 3 × 3 $cm^2$ with a 6-MV photon beam. The dose measured by the MOSFET detector was verified by the dose calculations of the superposition (SP) algorithm in the XiO radiotherapy treatment-planning system. In most cases, the measured doses agreed with the results of the SP algorithm within ±3%. Our results demonstrated the utility of the MOSFET detector for in vivo dosimetry even in the presence of clinical tissue inhomogeneities.

**Keywords** MOSFET detector · In vivo dosimetry · Anthropomorphic phantom · Inhomogeneity · Superposition algorithm

R. Kohno (✉) · E. Hirano · S. Kitou · T. Goka · S. Kameoka · T. Matsuura · T. Ariji · T. Nishio · M. Kawashima · T. Ogino
National Cancer Center Hospital East, 6-5-1 Kashiwanoha, Kashiwa, Chiba 277-8577, Japan
e-mail: rkohno@east.ncc.go.jp

R. Kohno
National Cancer Center Research Institute, 5-1-1 Tsukiji, Chuo-ku, Tokyo 104-0045, Japan

K. Matsubara
Graduate School of Human Health Sciences, Tokyo Metropolitan University, 7-2-10 Higashiogu, Arakawa-ku, Tokyo 116-8551, Japan

T. Matsuura
Foundation for Promotion of Cancer Research, 5-1-1 Tsukiji, Chuo-ku, Tokyo 104-0045, Japan

T. Nishio
Graduate School of Medicine, University of Tokyo, 7-3-1 Hongo, Bunkyo-ku, Tokyo 113-8655, Japan

Published online: 04 February 2010

## 1 Introduction

For implementation of radiation therapy with high-energy photon beams in the clinics, comprehensive dose verifications are essential. Generally, dose verifications on phantoms are recommended and carried out for each irradiation condition [1–4]. However, this does not mean that these verifications assure a perfect actual radiation dose to the patients. On the other hand, in vivo dosimetry can be used to identify major deviations in the delivery of treatment. Thus, we regard in vivo dosimetry during patient treatment as the ultimate dose verification for patient quality assurance (QA). Here, in order to carry out in vivo dosimetry, the detector must be very small, and easy to localize. To achieve this goal, we used metal oxide-silicon field-effect transistor (MOSFET) detectors (Best Medical Canada, Ottawa, Canada).

The MOSFET detector has a very small sensitive volume, which is a 0.2 mm × 0.2 mm, 0.5-μm-thick layer of insulating of silicon dioxide. The detector which we used is a dual-MOSFET detector consisting of two identical MOSFETs fabricated on the same silicon chip and operating at two different gate bias voltages, allowing temperature compensation of the detector response [5]. The MOSFET detector has been widely used for measuring radiation doses [6–11], and the accuracy, reliability, and usefulness of the MOSFET detector in clinical applications such as pinpoint absolute dosimetry has been reported [12].

An accurate estimate of the radiation dose is important for verifying that the expected dose of radiation has been delivered to the patient. Chuang et al. used a MOSFET detector in intensity-modulated radiation therapy (IMRT) dosimetric verification for routine IMRT phantoms, a solid water slab phantom, and a cylindrical PMMA phantom [7]. These dose verifications were performed on homogeneous materials. Carrasco et al. [13] measured percentage depth doses in inhomogeneous-layer phantoms containing water- and bone-equivalent materials using a MOSFET detector. The MOSFET detector was found suitable for dose measurement inside bone-equivalent materials. On the other hand, MOSFET detectors have previously been employed in surface dose measurements during in vivo dosimetry [8, 12, 14]. However, these measurements were not performed under the variable conditions created by inhomogeneous specimens containing water-, lung-, and bone-equivalent materials.

Here, we evaluated dose measurements using the MOSFET detector in inhomogeneous regular slab phantoms, as shown in "Appendix". The dose verification results for the superposition (SP) algorithm with use of the MOSFET detectors were similar to Kohno's results with use of the Farmer ionization chamber [15]. In general, the degree of accuracy in the dose measurement with MOSFET detectors is not as high as that with ionization chambers. However, we demonstrated that the MOSFET detector can measure doses with sufficient accuracy for various tissue-equivalent phantoms, various regular geometries, and various field sizes. From a different point of view, we can also say that it is important to measure dose independently using detectors with different characteristics, in order to evaluate the results of dose measurements in difficult irradiation conditions such as the presence of inhomogeneities.

On the other hand, the human body does not have a simple geometry such as the above regular slabs, and it forms complex inhomogeneities with bone, soft tissue, various materials, and various shapes. Therefore, it may not be certain that the results of dose verifications for slab-based phantoms can be extrapolated to actual clinical cases. In this paper, to evaluate the usefulness of the MOSFET detector as an in vivo dosimeter under more realistic conditions, we performed in vivo dosimetry using an anthropomorphic phantom.

## 2 Materials and methods

### 2.1 Experimental apparatus

Experiments were carried out with a Siemens ONCOR linear accelerator (Siemens Medical Solutions USA, Concord, CA) with a dual-focus, multi-leaf collimator. The specified uncertainty of the leaf positions was ±1 mm. For dose measurements, we used TN-502RD MOSFET detectors and the mobileMOSFET reader, set at the standard bias sensitivity. The MOSFET and a calibrated 0.6 cc Farmer ionization chamber type 30013 (PTW, Freiburg, Germany) were placed in a dose calibration phantom made of PMMA. Tough Water phantoms manufactured by Kyoto Kagaku Co., Ltd (Kyoto, Japan) were stacked on the dose calibration phantom. With a 6-MV photon beam at a dose rate of 300 MU/min, a dose of 100 MU was delivered at 100 cm source-to-axis distance (SAD), at a depth of 10 cm within a field of $10 \times 10$ cm$^2$ for calibration of the MOSFET response.

Measurements were carried out for simple square field sizes of $10 \times 10$, $5 \times 5$, and $3 \times 3$ cm$^2$ with a 6-MV photon beam. All measurement points were set in the center of an exposed square area. We used a beam angle of 0° for all of the experiments, thus avoiding uncertainties (~2%) of angular dependence [7, 11] of the MOSFET detector in the dose measurements, and unnecessary complexities in the SP dose calculations. We estimated the reproducibility as ±1.5% (1 standard deviation) for five consecutive irradiations of 100 MU each.

### 2.2 Anthropomorphic phantom

The RANDO anthropomorphic phantom (The Phantom Laboratory, Salem, CA) [16] provides a detailed mapping of the dose distribution that is essential for evaluating radiotherapy treatment plans. RANDO phantoms are constructed with a natural human skeleton cast inside a material that is radiologically equivalent to soft tissue. The RANDO lungs are molded to fit the contours of the natural human rib cage. The properties of the RANDO materials are listed in Table 1. The $\rho_{\text{nominal}}$ value is the nominal electron density relative to water for tissue-equivalent materials. Physical densities and effective atomic numbers of the tissue-equivalent materials are also shown in Table 1. The MOSFET detectors were placed within cavities in the phantom.

First, the detector positions were selected in the abdominal region. As shown in Fig. 1a and b, the abdominal region in the phantom is homogeneous. The measurement point is indicated by a cross mark, and the measurement depths for Fig. 1a and b were 6 and 9.5 cm, respectively.

Next, the dose measurement points for the chest region are illustrated in Fig. 2a–c. Figure 2a depicts a region of the mediastinum, which is a soft tissue. This measurement point is at an interface of the mediastinum and lung, with the beam central axis in the interface. On the other hand, Fig. 2b and c is in the lung region, and thus we were able to

**Table 1** Electron densities relative to water obtained by CT number conversion ($\rho_{meas}$), effective atomic number, and physical densities of the tissue-equivalent materials in the RANDO phantom used in this study

| Phantom | Soft tissue | Lung |
|---|---|---|
| $\rho_{nominal}$ | 0.979 | 0.311 |
| $\rho_{meas}$ | 1.014 ± 0.003 | 0.231 ± 0.015 |
| Effective atomic number | 7.60 | 7.11 |
| Physical density (g/cm$^3$) | 0.997 | 0.352 |

$\rho_{nominal}$ nominal electron density relative to water

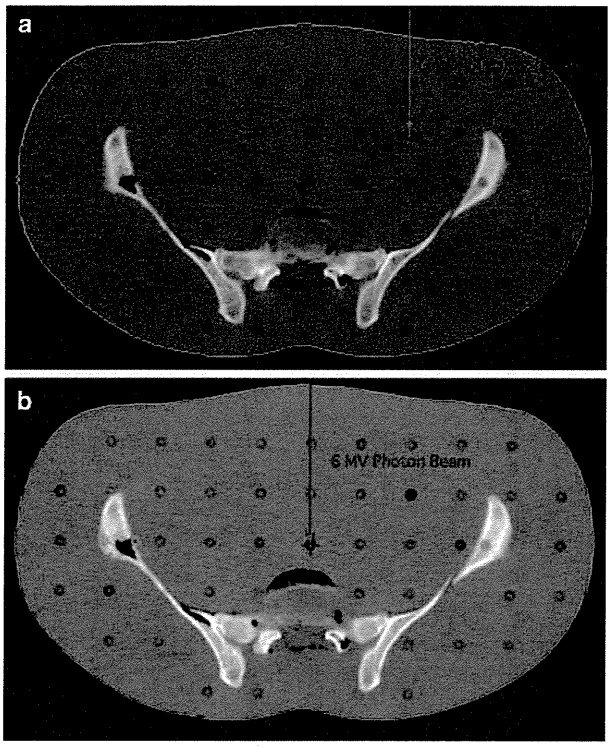


**Fig. 1** The homogeneous abdominal region of the anthropomorphic phantom. The measurement point is indicated by a *cross mark*, and the measurement depths for **a** and **b** were 6 and 9.5 cm, respectively. Measurements were carried out for simple square field sizes of 10 × 10, 5 × 5, and 3 × 3 cm$^2$ and a beam angle of 0° with a 6-MV photon beam. All measured points were set in the center of an exposed square area

evaluate the dose for low-density material. The measurement depths for Fig. 2b and c were 4.5 and 7.5 cm, respectively.

Figure 3a, b, and c illustrates measurement locations in the head and neck region. In Fig. 3a, the dosimeter is located at the center of the posterior arch of the first cervical vertebra in the RANDO phantom. The dose here was formed by the photon beam passing through the jaw, consisting of cortical bone, and the oral cavity, consisting of air. Figure 3b is the location posterior to the sella in the RANDO phantom, which corresponds to the surface of the brainstem. This region also consists of bone, cavities, and soft tissue, and forms complex inhomogeneities. Because of the presence of many critical structures, it is important to deliver accurate doses in this region. Figure 3c is a location posterolateral to the posterior arch of the first cervical vertebra.

## 2.3 Dose calculation and data analysis

The XiO 4.33.02 radiotherapy planning (RTP) system for dose calculations was used in this study. Doses were calculated using SP algorithm [17] with inhomogeneity correction. Here, the Monte Carlo (MC) method as a dose calculation algorithm is a powerful tool for analytic calculations and for verification of results obtained in difficult measurements situations. However, because the MC has considerable difficulties and uncertainties in reconstructive techniques based on measured depth dose distributions for clinical photon beams [18], we did not use it in this study. On the other hand, the SP has already been verified for various irradiation conditions by many authors [15, 17–21, "Appendix"] and has been widely adopted in clinical use. Therefore, using the SP as a dose calculation algorithm is reasonable for comparing the calculation dose with the MOSFET dose in this study. Three-dimensional dose distributions were calculated with 0.2 cm resolution.

Phantom information was obtained from computed tomography (CT) images. The CT images of all phantoms were acquired with an Asteion (Toshiba Medical Systems Corp., Tokyo, Japan) CT scanner at a 2.5 mm slice thickness and 2.5 mm slice separation. The electron density of each tissue, $\rho_{meas}$, is obtained by CT number conversion, and we used this value obtained by CT scan in our dose calculations. Here, the $\rho_{meas}$ of the lung material in Table 1 was somewhat smaller than the $\rho_{nominal}$. We assume that the lung material of the RANDO phantom changed over time. This may have led to overestimates in the dose calculations.

Dosimetric magnitudes were analyzed in terms of absolute doses. $D_{calc}$ is the calculated dose at a measurement point in the phantom, and $D_{meas}$ is the measured dose at the same point. The dose measured at each point was compared to the calculated dose, and the discrepancy at the measurement point, $\delta(\%)$, was evaluated as a percentage of the measured dose:

$$\delta(\%) = \frac{D_{calc} - D_{meas}}{D_{meas}} \times 100.$$

The error bars in each figure represent the reproducibility of the MOSFET dose.

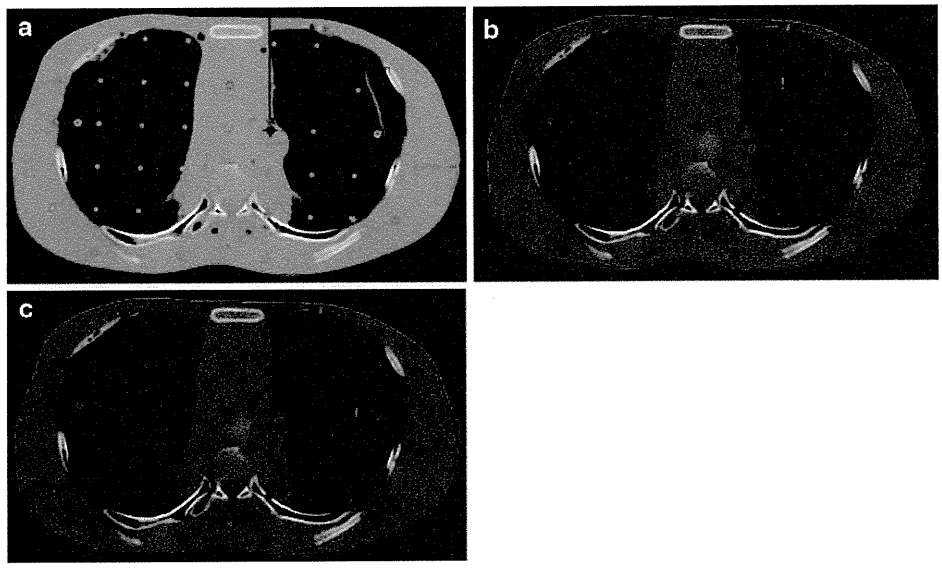


**Fig. 2** The chest region of the anthropomorphic phantom. The *cross marks* represent the measurement point. **a** A region of the mediastinum. **b** and **c** The lung region. The measurement depths for **b** and **c** were 4.5 and 7.5 cm, respectively. Measurements were carried out for simple square field sizes of 10 × 10, 5 × 5, and 3 × 3 $cm^2$ and a beam angle of 0° with a 6-MV photon beam. All measured points were set in the center of an exposed square area

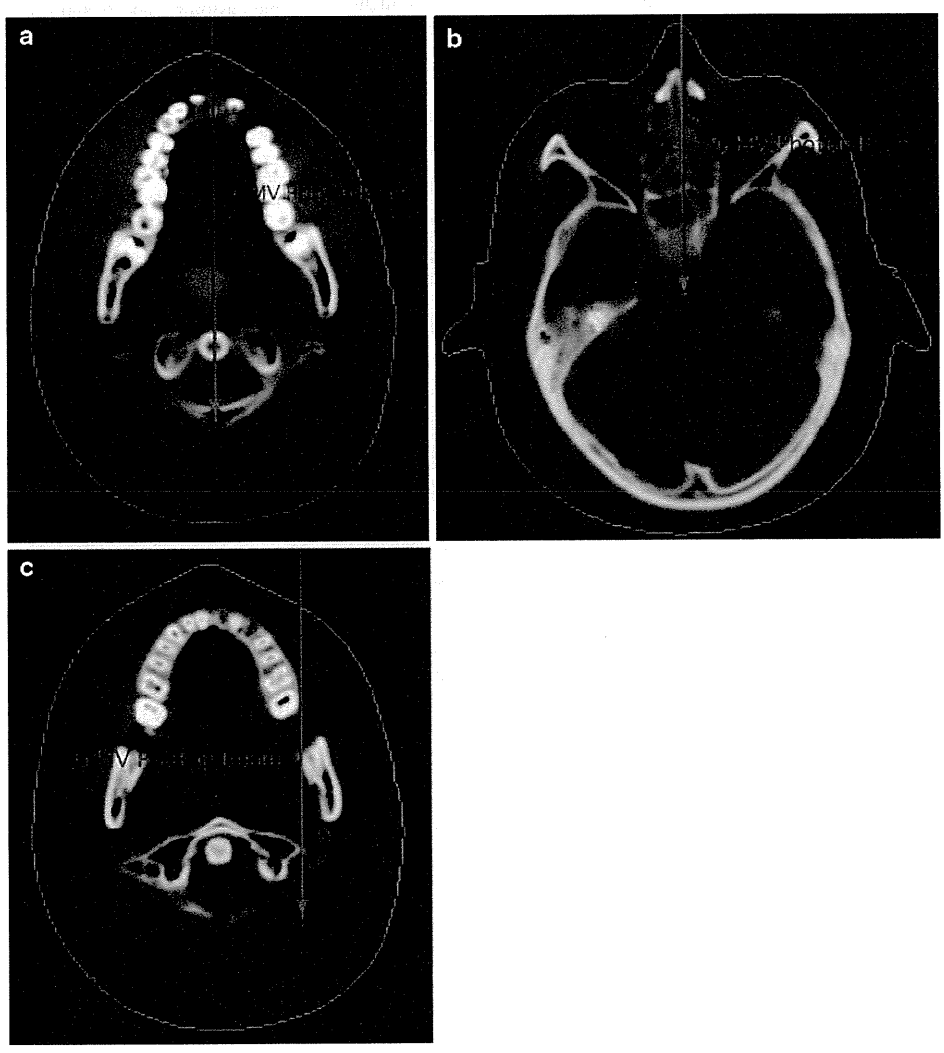


**Fig. 3** The head and neck region of the anthropomorphic phantom. The *cross marks* represent the measurement point. **a** The dosimeter is located at the center of the posterior arch of the first cervical vertebra in the RANDO phantom. **b** The location posterior to the sella in the RANDO phantom. **c** A location posterolateral to the posterior arch of the first cervical vertebra. Measurements were carried out for simple square field sizes of 10 × 10, 5 × 5, and 3 × 3 $cm^2$ and a beam angle of 0° with a 6-MV photon beam. All measured points were set in the center of an exposed square area

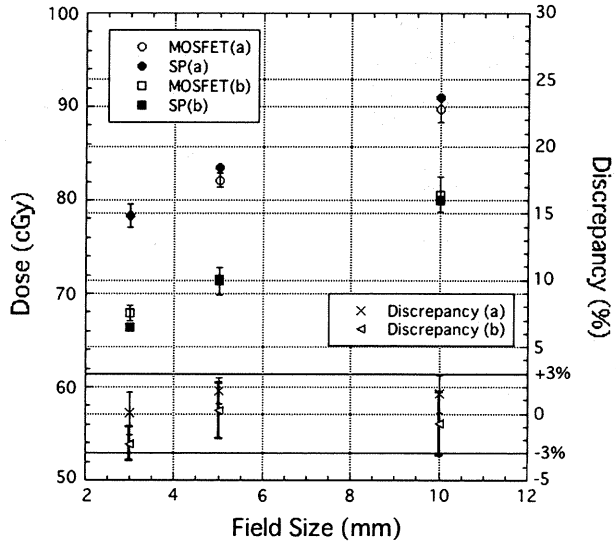


**Fig. 4** Comparisons between the doses measured with the MOSFET detector and doses calculated by use of the SP algorithm for the homogeneous abdominal region of Fig. 1. The measurement depths for **a** and **b** were 6 and 9.5 cm, respectively. This figure also includes the discrepancy (%) between doses measured with the MOSFET detector and doses calculated with the SP algorithm

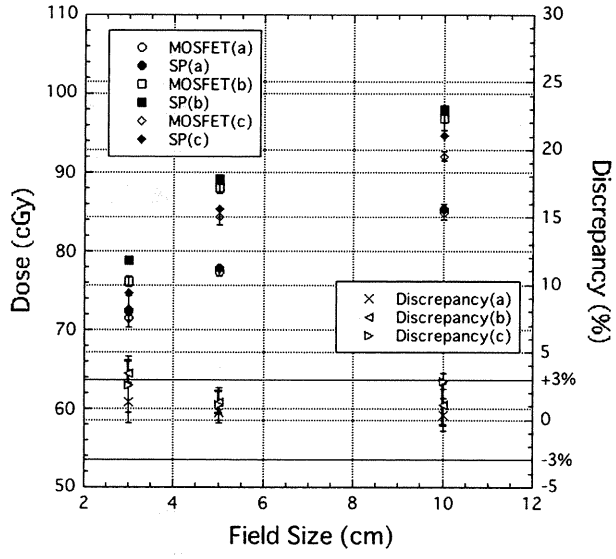


**Fig. 5** Comparisons between the doses measured with the MOSFET detector and doses calculated by use of the SP algorithm for the chest region of Fig. 2. Evaluation point (Fig. 2**a**) is a region of the mediastinum, and **b** and **c** are in the lung region. The measurement depths for Figs 2**b** and **c** were 4.5 and 7.5 cm, respectively. This figure also includes the discrepancy (%) between doses measured with the MOSFET detector and doses calculated with the SP algorithm

## 3 Results and discussion

Figure 4 contains comparisons between doses measured with the MOSFET detector and doses calculated by the SP method for soft tissue for Fig. 1a and b, respectively. This figure also includes the discrepancy (%) between doses measured with the MOSFET detector and doses calculated with the SP algorithm. The measured doses agreed with the results of the SP algorithm within ±3%.

Comparisons between the measurements and calculations for the chest region (Fig. 2a–c) are displayed in Fig. 5. We observed that the SP overestimates the dose particularly in the lung region (Fig. 2b, c) compared with the measurements. We can explain this by an underestimation by use of the relative electron density for lung material, as shown in Table 1. Then, the difference of the doses between MOSFET and SP at a field size of 3 cm is larger than those at 5 and 10 cm. Because the leaf position uncertainty of ±1 mm contributes approximately 0.5% to the dose uncertainty for the 3 × 3 $cm^2$ field size, it may be one of the causes of the larger difference.

Figure 6 depicts comparisons between doses measured with the MOSFET detector and doses calculated with the SP algorithm for the head and neck measurements mapped in Fig 3a–c. Here, Kohno et al. [15] reported that a definite deterioration in the dose prediction accuracy occurred when they used the SP algorithm in bone material for a field size of 3 × 3 $cm^2$. Moreover, Fig. 8c also supported the deterioration. Therefore, the SP algorithm would display significant differences in Fig. 3a due to the inadequate energy deposition kernel model for bone material [19]. However, even in this complex inhomogeneous region, the measured doses agreed with the results of the SP algorithm within ±3%. We concluded that the actual body does not include large and thick bones such as this in Fig. 7c, which results in a large deterioration of the dose prediction due to the incomplete energy deposition kernel model in the photon dose calculation.

Thus, dose measurements by use of the MOSFET detector were compared with calculations by the SP algorithm for various irradiation conditions. The small size, immediate read-out, and fast response of the MOSFET detector make it particularly useful for dose measurements for therapeutic MV photon beams. The results of our dosimetric measurements demonstrate the utility of the MOSFET detector for clinical dosimetry in radiotherapy. Our dose measurements were performed at a beam angle of 0°. Given the variety of beam angles used in actual radiotherapy, the ±2% angular dependence of the MOSFET detector must be considered [7, 11]. The angular dependence may lead to a decrease in accuracy at some angles, which, in turn, may affect the clinical utility of this detector.

## 4 Conclusion

We evaluated in vivo dosimetry with a MOSFET detector for an anthropomorphic phantom. Dose measurements

were carried out in the abdominal, thoracic, and head and neck regions for simple square field sizes of 10 × 10, 5 × 5, and 3 × 3 $cm^2$ with a 6-MV photon beam. The measured dose agreed with the results obtained with the SP algorithm to within ±3%. The MOSFET detector as an in vivo dosimeter was useful for pinpoint absolute dosimetry even in the presence of clinical tissue inhomogeneities.

**Acknowledgments** The authors would like to express their gratitude to A. Hallil of Best Medical Canada Ltd. for his technical advice and support. The authors also thank Yu Furuhata, AcroBio Corporation, for his support.

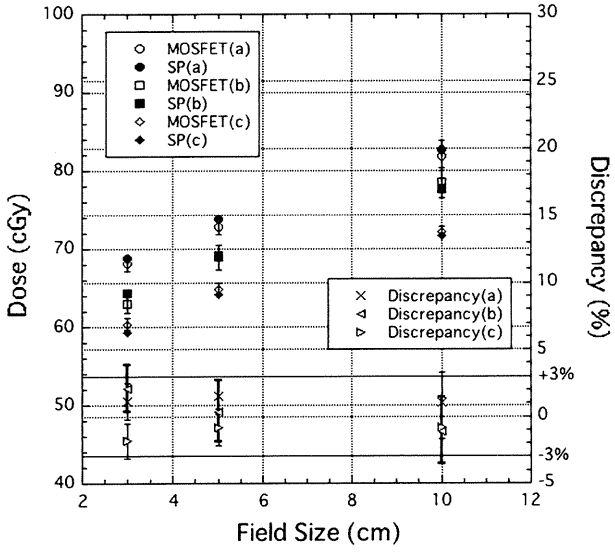


**Fig. 6** Comparisons between the doses measured with the MOSFET detector and doses calculated by use of the SP algorithm for the head and neck region of Fig. 3. The dosimeter of Fig. 3 is located at the center of the posterior arch of the first cervical vertebra. Figure 3**b** and **c** are the location posterior to the sella and the location of posterolateral to the posterior arch of the first cervical vertebra. This figure also includes the discrepancy (%) between doses measured with the MOSFET detector and doses calculated with the SP algorithm

## Appendix

### Evaluation of dose measurements by use of a MOSFET detector in inhomogeneous slab phantoms for 6 MV photon beam (Figs. 7, 8, 9, and 10)

We summarize the dose evaluations by use of the MOSFET detector in multi-layer and laterally inhomogeneous phantoms, the geometries of which were the same as those in the study of Kohno et al. [15]. Doses measured by the MOSFET detector were compared to these point doses calculated by the SP algorithm with inhomogeneity correction in the same RTP system. Experiments were carried out with the same beam conditions, 6 MV, dose rate of 300 MU/min, beam angle of 0°, and square field sizes of 10 × 10, 5 × 5, and 3 × 3 $cm^2$. A dose of 100 MU was delivered 5 times at 100 cm SAD. In these measurements, a tough water phantom (TW), tough lung phantom (TL), tough bone BE-H phantom (TB) (Kyoto Kagaku Co., Ltd, Kyoto, Japan), and a PMMA phantom were used (Table 2).

Figure 7 illustrates the layout of the TW and PMMA phantoms for the TW, TL, and TB thicknesses of 9 cm (a), 9 cm (b), and 4 cm (c). These phantom geometries can be used for checking the dose levels beyond a lung or bone

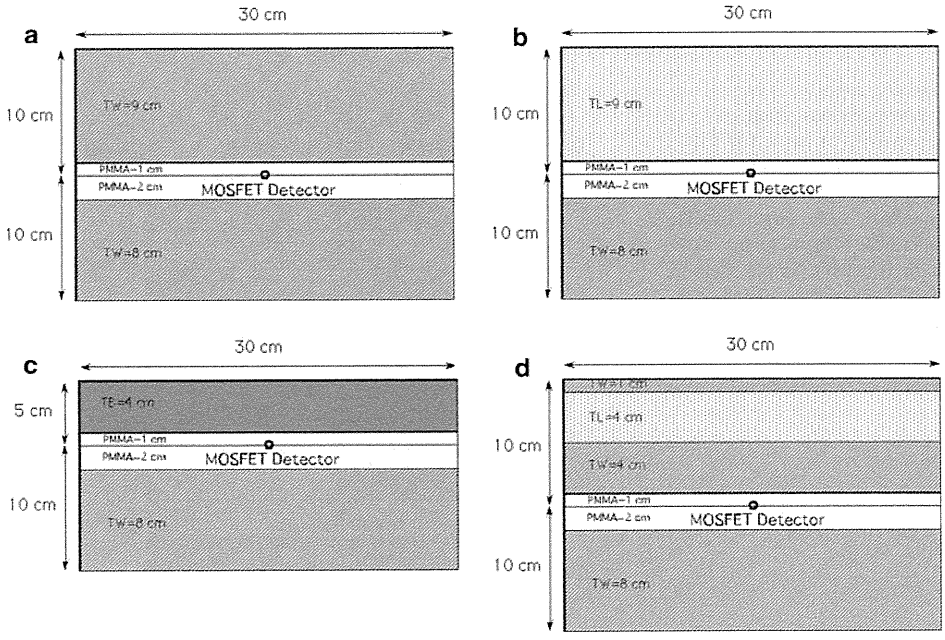


**Fig. 7** Multi-layer phantom geometries of the **a** TW and PMMA phantoms for TW thicknesses of 9 cm, **b** TL phantom with a thickness of 9 cm, **c** TB phantom with a thickness of 4 cm, and **d** TW + TL + TW phantom. Measurements were carried out for simple square field sizes of 10 × 10, 5 × 5, and 3 × 3 $cm^2$ and a beam angle of 0° with a 6-MV photon beam

structure. Figure 7d demonstrates the typical geometry of a thoracic wall-lung-thoracic wall interface.

Figure 8 shows a comparison between doses measured with the MOSFET detector and doses calculated with the SP algorithm for the phantoms of Fig 7. This figure also includes a discrepancy (%) of doses measured with the MOSFET detector and doses calculated with the SP algorithm. The measured results for the (a) TW 9 cm and the (b) TL 9 cm phantom were within 1.5% of the corresponding calculation. For the (c) TB 4 cm phantom, the measured results were within 2.5% of the calculated values for field sizes of 10 × 10 and 5 × 5 $cm^2$. However, for a field size of 3 × 3 $cm^2$, the dose measurement underestimated the calculated dose by 5.5%. Although the difference increased with decreasing field size, the leaf position uncertainty of ±1 mm may have contributed approximately 1% to the dose uncertainty for the 3 × 3 $cm^2$ field size. However, this cannot account for the entire uncertainty. This discrepancy is comparable to that reported by Kohno et al. [15]; therefore, we estimated that this is because the bone material is equivalent to water (i.e., has the same atomic properties) in the dose calculation [19]. In fact, electrons released in materials with higher atomic numbers are scattered at wider angles compared to electrons generated in water. For the (d) TW + TL + TW phantom, the results at a point beyond a typical thoracic wall-lung-thoracic wall interface from the MOSFET measurements agreed with the SP calculations to around 3% for each field size.

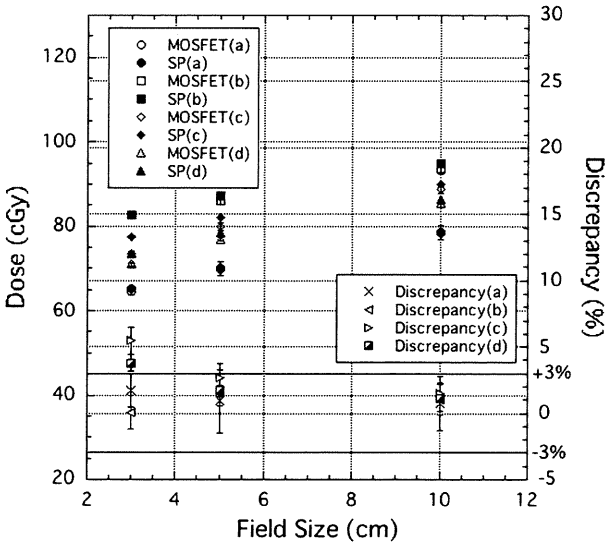


**Fig. 8** Comparisons between the measurement dose from a MOSFET detector and doses calculated using the SP algorithms for the multilayer phantom geometries of the Fig 1**a** TW 9 cm, **b** TL 9 cm, **c** TB 4 cm, and **d** TW + TL + TW phantom. This figure also includes discrepancy (%) of doses measured with the MOSFET detector and doses calculated with the SP algorithm

Figure 9a–c depicts the three laterally inhomogeneous phantom geometries. Figure 9a and b model a mediastinum/lung interface with the beam central axis in the interface. Figure 9c represents a TB/TL interface. For these configurations, because we expected the phantom setups to have a considerable effect on the dose at the measurement point, each dose measurement was performed independently twice.

Figure 10 depicts the measured and calculated absolute doses for each laterally inhomogeneous phantom, as well as the dose profile calculated by the SP algorithm, because the measurement point has a gradient dose distribution in the lateral direction. From this dose profile, we can estimate the effect of the phantom setup uncertainty.

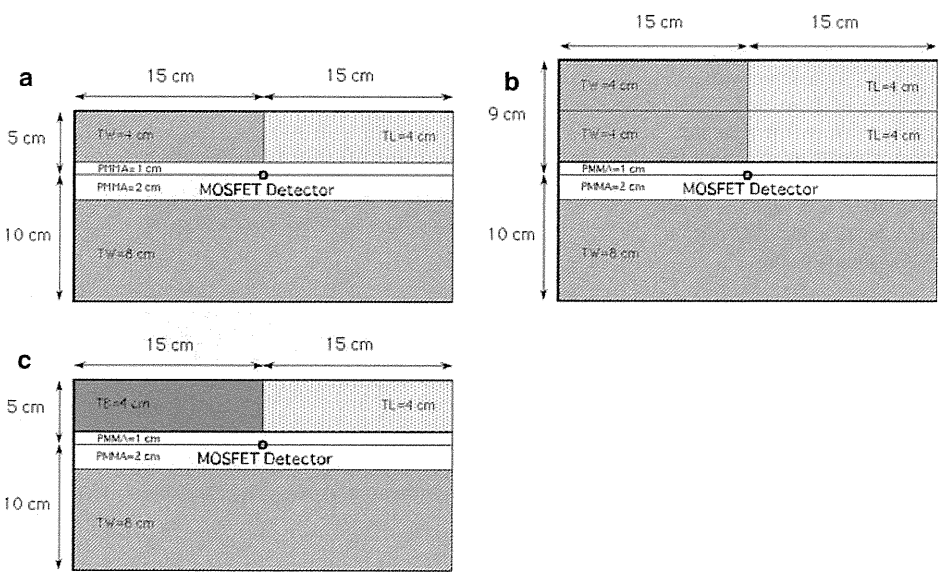


**Fig. 9** Laterally inhomogeneous phantom geometries of the **a** TW/TL interface with the beam central axis in the interface, **b** TB/TL interface, and **c** larger TW/TL interface. Measurements were carried out for simple square field sizes of 10 × 10, 5 × 5, and 3 × 3 $cm^2$ and a beam angle of 0° with a 6-MV photon beam

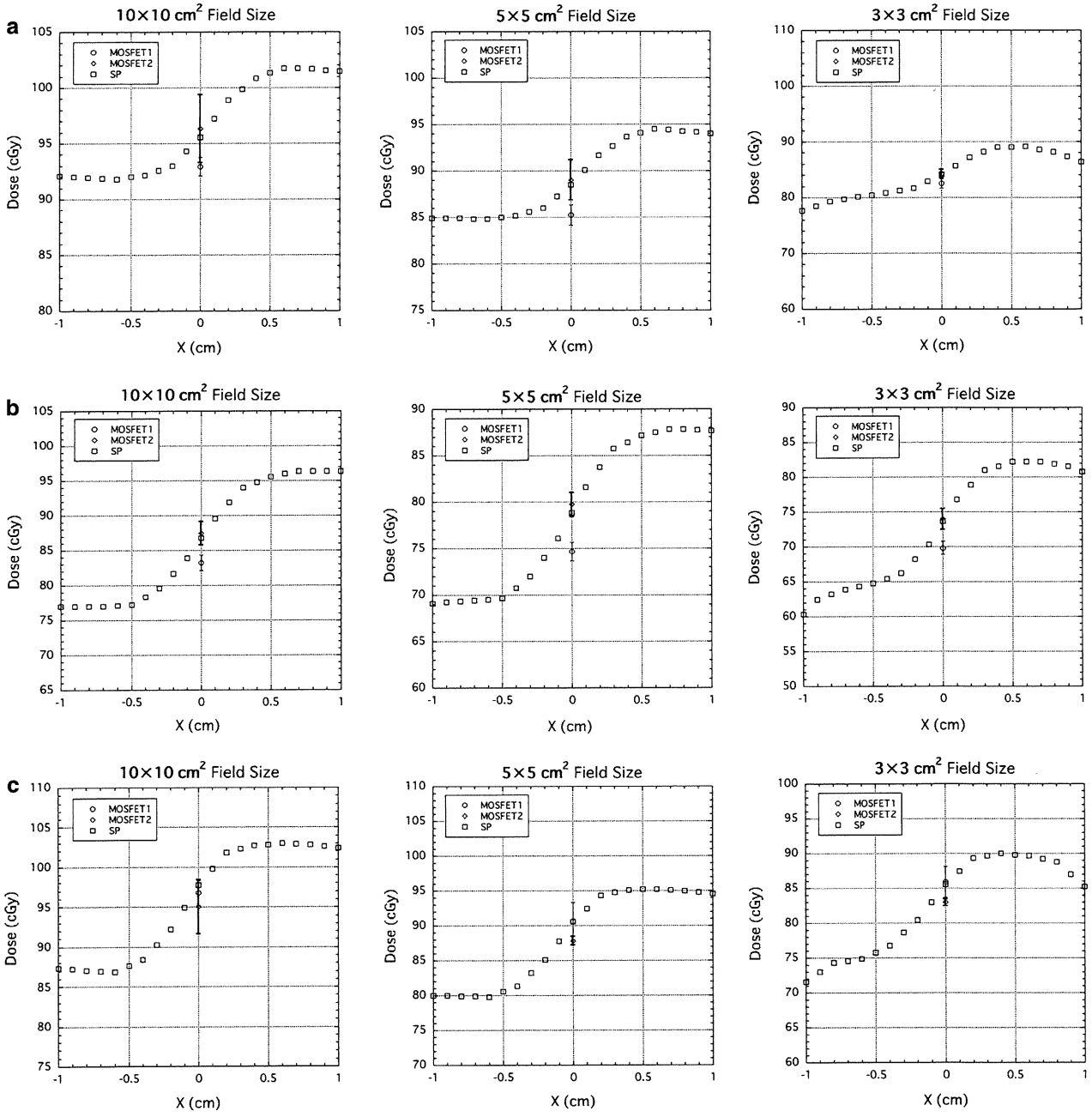


**Fig. 10** Comparisons between the measurement dose from a MOSFET detector and doses calculated using the SP algorithm for the laterally inhomogeneous phantom geometries of the Fig 2a TW/TL interface, b TB/TL interface, and c larger TW/TL interface. This figure also includes the dose profile calculated by the SP algorithm

Figure 10a and b depicts the measured and calculated absolute doses at the TW/TL interface, and the measurement points had a gradient dose distribution of 1.5–5%/mm in the lateral direction. Most results agreed with the SP calculations within 3%. Although the maximum difference was +5.6% for a field size of 5 × 5 $cm^2$ in Fig. 10b, we could explain this large difference as the effect of the phantom setup uncertainty of ±1 mm. Thus, this highlights the difficulty in point dose measurement with a small radiation detector. The measured and calculated doses for the TB/TL interface are plotted in Fig. 10c. The results of the MOSFET measurement agreed with the SP calculations within 3%, in spite of the fact that the measurement point had a gradient dose distribution of 3%/mm in the lateral

**Table 2** Electron densities relative to water obtained by CT number conversion ($\rho_{meas}$), effective atomic number, and physical densities of the tissue-equivalent materials used in this study

| Phantom | Tough water | Tough lung | Tough bone | PMMA |
|---|---|---|---|---|
| $\rho_{nominal}$ | 0.990 | 0.313 | 1.416 | 1.148 |
| $\rho_{meas}$ | 1.013 ± 0.006 | 0.320 ± 0.023 | 1.395 ± 0.003 | 1.137 ± 0.006 |
| Effective atomic number | 7.44 | 7.77 | 11.70 | 6.47 |
| Physical density (g/cm$^3$) | 1.017 | 0.320 | 1.500 | 1.190 |

$\rho_{nominal}$ nominal electron density relative to water

direction. The kernel model for bone material in the SP algorithm did not significantly affect the dose accuracy in this case.

Doses measured by the MOSFET detector in inhomogeneous regular slab phantoms were compared to those calculated by the SP algorithm in the XiO radiotherapy treatment-planning system. Except for the TB phantom at the small field size, the results of the MOSFET detector agreed with the calculated doses to within 3%. We reconfirmed and support the results of Kohno's study [15] with dose measurements with the MOSFET detector. The MOSFET detector was useful for pinpoint dosimetry even in inhomogeneous slab media.

## References


1. Nishio T, Kohno R, Mori S, Mizuno H, Hanyu Y, Takahashi Y. Quality assurance of treatment planning systems for X-ray beams. Jpn J Med Phys. 2008;27(6).
2. IAEA Technical Reports Series No. 430. Comissioning and quality assurance of computerized planning systems for radiation treatment of cancer. Vienna: IAEA; 2005.
3. Fraass B, Doppke K, Hunt M, Kutcher G, Starkschall G, Stern R, et al. Quality assurance for clinical radiotherapy treatment planning. Med Phys. 1998;25:1773–829.
4. ESTRO Booklet No. 7. Quality assurance of treatment planning systems practical examples for non-IMRT photon beams. Brussels: ESTRO; 2004.
5. Soubra M, Cygler J, Mackay G. Evaluation of a dual bias dual metal oxide-silicon semiconductor field effect transistor detector as radiation dosimeter. Med Phys. 1994;21:567–72.
6. Ramaseshan R, Kohil KS, Zhang TJ, Lam T, Norlinger B, Hallil A, et al. Perfomance characteristics of a microMOSFET as an in vivo dosimeter in radiation therapy. Phys Med Biol. 2004; 49:4031–48.
7. Chuang CF, Verhey LJ, Xia P. Investigation of the use of MOSFET for clinical IMRT dosimetric verification. Med Phys. 2002;29:1109–15.
8. Ramaseshan R, Stephen R, Peter O. Clinical dosimetry using MOSFETs. Int J Radiat Oncol Biol Phys. 1997;37:959–64.
9. Kohno R, Nishio T, Miyagishi T, Hirano E, Hotta K, Kawashima M, et al. Experimental evaluation of a MOSFET dosimeter for proton dose measurements. Phys Med Biol. 2006;51:6077–86.
10. Gurp EJB, Minken AWH, Mijnheer BJ, Dehing-Oberye CJG, Lambin P. Clinical implementation of MOSFET detectors for dosimetry in electron beams. Radiother Oncol. 2006;80:288–95.
11. Kohno R, Hirano E, Nishio T, Miyagishi T, Goka T, Kawashima M, et al. Dosimetric evaluation of a MOSFET detector for clinical application in photon therapy. Radiol Phys Technol. 2008; 1:55–61.
12. Marcie S, Charpiot E, Bensadoun RJ, Ciais G, Herault J, Costa A, et al. In vivo measurements with MOSFET detectors in oropharynx and nasopharynx intensity-modulated radiation therapy. Int J Radiat Oncol Biol Phys. 2005;61:1603–6.
13. Carrasco P, Jornet N, Duch MA, Panettieri V, Weber L, Eudaldo T, et al. Comparison of dose calculation algorithms in slab phantoms with cortical bone equivalent heterogeneities. Med Phys. 2007;34:3323–33.
14. Cherpak A, Studinski RCN, Cygler JE. MOSFET detectors in quality assurance of tomotherapy treatments. Radiother Oncol. 2008;86:242–50.
15. Kohno R, Kitou S, Hirano E, Kameoka S, Goka T, Nishio T, et al. Dosimetric verification in inhomogeneous phantom geometries for the XiO radiotherapy treatment planning system with 6 MV photon beams. Radiol Phys Technol. 2009;2:87–96.
16. Kleck JH, Smathers JB, Holly FE, Myers LT. Anthropomorphic radiation therapy phantoms: a quantitative assessment of tissue substitutes. Med Phys. 1990;17:800–6.
17. Miften M, Wiesmeyer M, Monthfer S, Krippner K. Implementation of FFT convolution and multigrid superposition models in the FOCUS RTP system. Phys Med Biol. 2000;45:817–33.
18. AAPM report No. 85. Tissue inhomogeneity corrections for megavoltage photon beams. Madison: Medical Physics Publishing; 2004.
19. Miften M, Wiesmeyer M, Kapur A, Ma CM. Comparison of RTP dose distributions in heterogeneous phantoms with the BEAM Monte Carlo simulation system. J Appl Clin Med Phys. 2001; 67:21–31.
20. Garcia-Vicente F, Minambres A, Jerez I, Modolell I, Torres JJ. Experimental validation tests of fast Fourier transform convolution and multigrid superposition algorithms for dose calculation in low-density media. Radiother Oncol. 2003;67:239–49.
21. Fogliata A, Vanetti E, Albers D, Brink C, Clivio A, Knoos T. et al. On the dosimetric behaviour of photon dose calculation algorithms in the presence of simple geometric heterogeneities: comparison with Monte Carlo calculations. Phys Med Biol. 2007;52:1363–85.

Japanese Journal of Clinical Oncology Advance Access published December 22, 2010

JJCO Japanese Journal of Clinical Oncology

*Jpn J Clin Oncol 2010*
*doi:10.1093/jjco/hyq231*

**Original Article**

# Long-term Outcomes of Fractionated Stereotactic Radiotherapy for Intracranial Skull Base Benign Meningiomas in Single Institution

**Shunsuke Onodera[1,*], Hidefumi Aoyama[1], Norio Katoh[1], Hiroshi Taguchi[1], Kouichi Yasuda[1], Daisuke Yoshida[1], Ken Surtherland[2], Ryusuke Suzuki[2], Masayori Ishikawa[2], Bengua Gerard[2], Shunsuke Terasaka[3] and Hiroki Shirato[2]**

[1]Department of Radiation Medicine, Hokkaido University Graduate School of Medicine, [2]Department of Medical Physics, Hokkaido University Graduate School of Medicine and [3]Department of Neurosurgery, Hokkaido University Graduate School of Medicine, Sapporo, Japan

*For reprints and all correspondence: Shunsuke Onodera, Department of Radiation Medicine, Hokkaido University Graduate School of Medicine, North 15, West 7, Kita-ku, Sapporo 060-8638, Japan. E-mail: m950086@jasmine.ocn.ne.jp

Received May 6, 2010; accepted November 21, 2010

**Objective:** To investigate the outcome of linac-based fractionated stereotactic radiotherapy over the last 10 years for intracranial skull base benign meningiomas in patients who were inoperable, who had residual tumors with some components of high mitotic index after surgery and who experienced relapse of the tumor.

**Methods:** Twenty-seven patients with intracranial skull base benign meningiomas treated with fractionated stereotactic radiotherapy were retrospectively reviewed. Twenty-seven cases were diagnosed as benign meningiomas on pathological (17 cases) or radiological (10 cases) examination. The median follow-up time was 90 months after initial treatment and 63 months after fractionated stereotactic radiotherapy. The median biological equivalent dose calculated using an $\alpha/\beta$ ratio of 2.0 Gy was 82.0 Gy (range, 60–106 Gy).

**Results:** The 5-year overall survival was 95.7 (95% confidence interval: 87.3–100)% after initial treatment and 96.2 (88.8–100)% after fractionated stereotactic radiotherapy. The 5-year overall survival and local control rate of patients who received fractionated stereotactic radiotherapy alone were both 100%. The 5-year progression-free survival and local control rate after fractionated stereotactic radiotherapy were all 100% with a tumor volume of <9.1 cc and 68.2 (37.2–99.2) and 75.8 (45.2–100)% for the tumors 9.1 cc, respectively. The difference was significant in progression-free survival ($P = 0.022$) and local control rate ($P = 0.044$). The local control rate was significantly worse in patients who received fractionated stereotactic radiotherapy for relapsed tumors ($P = 0.01$). No late radiation damage was observed in the follow-up period.

**Conclusions:** The long-term outcome suggests that fractionated stereotactic radiotherapy is a safe and effective treatment for intracranial skull base benign meningioma, especially for those who have tumors <9.1 cc or would receive fractionated stereotactic radiotherapy with or without surgery as the initial treatment.

*Key words: radiation therapy – meningioma – stereotactic – skull base – fractionation*

## INTRODUCTION

Radiotherapy is increasingly being used for the treatment of meningiomas after incomplete resection, after recurrence and when tumor histology is atypical or malignant (1,2). When meningiomas are located in the intracranial skull base region, tumor excision is frequently incomplete and even

biopsy can be hazardous (1). Therefore, it is a matter of debate whether the use of radiotherapy should be used when the residual tumor is still small as the primary treatment or should be reserved as a potential salvage treatment for the residual tumor enlarged (3).

Stereotactic radiosurgery (SRS) has been proven useful for reducing unnecessary irradiation to the normal tissue surrounding meningiomas and provides an excellent local control rate (LCR) for small to mid-size skull base meningiomas (3,4). Three-dimensional conformal radiotherapy (3D-CRT) and fractionated stereotactic radiotherapy (FSRT) are expected to be useful for further reducing the possibility of late adverse reactions, even for relatively large tumors (5,6). Although there were several precise reports from a few institutions about the long-term outcome after FSRT (5–8), we are still short of knowledge about the treatment results of FSRT with the median follow-up longer than 60 months for intracranial meningioma.

We began using FSRT 15 years ago for patients with intracranial skull base meningiomas, principally for patients who were inoperable, who had residual tumors with some components of high mitotic index or high MIB-1 index, who experienced relapse of the tumor. In this study, we retrospectively reviewed our long-term results for FSRT of intracranial skull base benign meningiomas in order to investigate the usefulness and prognostic factors of this treatment.

## PATIENTS AND METHODS

### Patients

The outcome of 27 patients with intracranial skull base benign meningiomas treated with FSRT at Hokkaido University Hospital between May 1994 and February 2009 was retrospectively reviewed. Our treatment policy was to apply FSRT principally for those patients with intracranial skull base meningiomas who were inoperable, who had residual tumors or who experienced relapse of the tumor.

The patients' characteristics are summarized in Table 1, which were classified by the treatment category. In our cases, diagnosis was based on pathological examinations in 17 patients and radiological characteristics in 10 patients. The tumor was located at lateral structures in 17 (anterior fossa in 2, middle-lateral sphenoid wing in 8 and cerebellopontine angle and posterior fossa in 7 patients) and at central structures in 10 patients (cavernous sinus and tuberculum sellae in all 10 patients). The median tumor volume was 9.1 (range: 1.1–86.1) cc in all benign meningiomas. The median tumor volume in the initial treatment group was smaller than that in the salvage treatment group (6.3 vs. 12.3 cc), but there was no significant difference statistically ($P = 0.139$; Mann–Whitney test).

In this study, 11 patients were treated with FSRT alone as the initial treatment: 1 after biopsy (Simpson's grade V) and 10 after radiological diagnosis. Radiotherapy was used as a part of the initial treatment after incomplete excision in 4 patients and as a salvage treatment for tumor recurrence after surgery in 12 patients. The number of surgical procedures before FSRT was 1, 2 and 3 in 10, 5 and 1 patients, respectively. Patients who received open biopsy or surgery were classified according to Simpson's grade (9). Simpson's grade II (complete removal and coagulation of dual attachment) and IV (subtotal resection) surgery before radiotherapy was performed in 1 and 15 patients, respectively. Only one patient received biopsy (Simpson's grade V).

**Table 1.** Patients' characteristics

| Factors | Initial treatment group | Salvage treatment group | Total |
|---|---|---|---|
| Total | 15 | 12 | 27 |
| Diagnosis | | | |
| Pathological diagnosis | 5 | 12 | 17 |
| Radiological diagnosis | 10 | 0 | 10 |
| Sex | | | |
| Male | 1 | 6 | 7 |
| Female | 14 | 6 | 20 |
| Age | | | |
| Mean (range) | 60.3 (18–78) | 45.5 (14–72) | 53.7 (14–78) |
| Tumor cite | | | |
| Lateral | 11 | 6 | 17 |
| Central | 4 | 6 | 10 |
| Gross tumor volume | | | |
| Median (range) (cc) | 6.3 (1.1–58.9) | 12.3 (2.5–86.1) | 9.1 (1.1–86.1) |
| Simpson's grade | | | |
| I | 0 | 0 | 0 |
| II | 0 | 1 | 1 |
| III | 0 | 0 | 0 |
| IV | 4 | 11 | 15 |
| V | 1 | 0 | 1 |
| Radiotherapy alone | 10 | 0 | 10 |

### Radiation Therapy Method

The gross tumor volume (GTV) was taken as the gross tumor shown on computed tomography (CT) with or without magnetic resonance imaging (MRI). The clinical target volume (CTV) was equal to the GTV, post-operative tumor bed or both in this study. The planning target volume (PTV) was 2–3 mm geometric expansion of the CTV. In delineating GTV, MRI co-registered with CT was used in 18 recent patients, and only the CT information was used for the remaining 9 patients.

Treatment planning systems were Focus or Xio (CMS Japan, Japan). A dose calculation algorithm used for the

skull base meningiomas was the Clarkson method or the convolution method. Stereotactic radiotherapy was carried out by using a 6 or 10 MV linear accelerator (LINAC) (2100C: Varian, Palo Alto, CA, USA; EXL15DP: Mitsubishi, Japan) with an in-house developed LINAC-based SRT system. Three-dimensional non-coplanar, single isocenter and the technique using multileaf collimator (MLC) were used. Three to eight static non-coplanar ports with the conformal fields were used in general. The width of these leafs was 5–10 mm at the isocenter. The dose was prescribed at the isocenter and defined as 100% in the dose distribution profile. MLCs were opened to cover PTV by a 90–95% isodose shell. The maximum dose point was always situated near the isocenter with the dose <110% (Fig. 1).

Patients were fixed by using a thermo-plastic mask and a custom-made head rest system. The dose to the optic chiasm was limited to ≤46 Gy. The total dose was 48–54 Gy in 26 cases and 32 Gy in 1 case using 2.0 Gy as the daily dose. When these radiation schedules were converted into the biological equivalent dose (BED) using an $\alpha/\beta$ ratio of 2.0 Gy, the median BED dose was 82.0 Gy (range: 52–90 Gy).

### Follow-up and Statistical Analyses

The median follow-up time was 90 months (range: 21–209 months) after initial treatment, surgery or FSRT. The median follow-up time was 63 months (range: 19–154 months) after FSRT. More than 70% of patients were followed longer than 36 months after FSRT. Patients were periodically monitored by physical as well as radiographic examination in Hokkaido University Hospital and related hospitals. Local tumor progression (PD) was scored when the maximum diameter of the tumor increased 2 mm or more and partial reaction was scored when the diameter decreased 2 mm or more. The LCR was defined as no change or decrease of the tumor volume in the anatomical region consistent with the PTV of the treatment planning image. When more than 80% of the relapsed tumor volume was outside of the PTV, the recurrence was defined as out of field (10). In-field (>95% of the relapsed tumor volume in the PTV), marginal (20–95% of the relapsed tumor volume in the PTV), and out-of-field (less than 20% of the relapsed tumor volume in the PTV) recurrence were defined in this study.

Statistical analyses were conducted by using commercially available software (SPSS v18; IBM Inc., Chicago, IL). The overall survival (OS) and LCR were calculated from the date of the initiation of radiotherapy using the Kaplan–Meier method, and statistical evaluations were carried out by the log-rank test.

## RESULTS

The OS, progression-free survival (PFS) and LCR at 5 years after initial treatment were 95.7 [95% confidence interval (CI): 87.3–100], 91.6 (80.4–100) and 95.5 (86.9–100)%.

The OS, PFS and LCR at 5 years after FSRT were 96.2 (88.8–100), 84.6 (67.7–100) and 88.6 (72.9–100)%.

Partial response was achieved in two benign patients, and the other patients with local control experienced no change of tumor volume. Three (11%) patients experienced in-field recurrence. These tumors had received Simpson's grade IV surgical resection. One patient had progression disease out of irradiation field. The recurrent cases were observed at the posterior fossa (at 55 and 81 months) in two patients, and at the cavernous sinus and tuberculum (at 19 and at 27 months) in two patients. These four recurrent cases are summarized in Table 2. No marginal recurrence was observed.

Univariate analyses were performed on OS, PFS and LCR after FSRT for patients with benign meningioma (Table 3). The female patients had significantly better PFS ($P = 0.009$) and LCR ($P = 0.04$) than the male patients. The 5-year OS, PFS and LCR after FSRT were all 100% for the benign meningiomas with a tumor volume of <9.1 cc and these parameters were 91.7 (76.0–100), 68.2 (37.2–99.2) and 75.8 (45.2–100)% for the tumors >9.1 cc, respectively. The difference was significant in PFS ($P = 0.022$) and LCR ($P = 0.044$) (Fig. 2).

In this study, the 11 patients who received FSRT alone had 100% OS, 88.9% PFS and 100% LCR at 5 years, respectively. The OS, PFS and LCR of patients who received FSRT with or without surgery as the initial treatment ($n = 15$) were 100, 91.7 and 100%, whereas those of patients who received FSRT for relapse ($n = 12$) were 90.9, 68.2 and 68.2%, respectively. The LCR was significantly worse in patients who received FSRT for a relapsed tumor ($P = 0.01$). A higher biological radiation dose, BED, was paradoxically associated with a lower PFS and LCR. The median tumor volume was larger (11.0 vs. 6.7 cc) and the ratio of patients with relapsed tumor was higher (7/11 vs. 5/16) in the higher

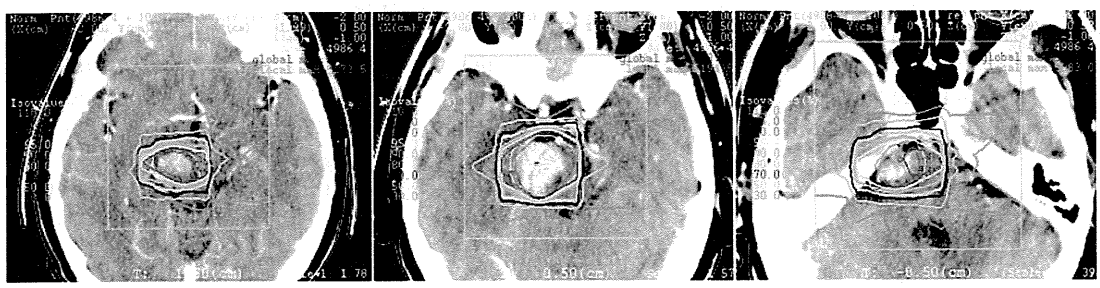

**Figure 1.** Dose distribution of FSRT for an intracranial benign meningioma. FSRT, fractionated stereotactic radiotherapy.